

Southern Hemisphere subtropical front impacts on Southern African hydroclimate across the Mid-Pleistocene Transition

Received: 28 June 2024

Accepted: 1 April 2025

Published online: 12 April 2025

 Check for updates

Claire B. Rubbelke¹  , Tripti Bhattacharya¹, Alexander Farnsworth^{2,3,6}, Paul Valdes^{2,3,6}, Erin L. McClymont^{4,6} & Heather Ford^{5,6}

Southern African (SA) hydroclimate is largely shaped by the interactions of atmospheric circulations, e.g., Hadley Circulation, and oceanic elements, like the Benguela Upwelling System (BUS), Agulhas System, and Antarctic Circumpolar frontal system. Large-scale changes to the Meridional Temperature Gradient (MTG) influence both the atmospheric and oceanic components of the hydroclimate system, and thus impact hydroclimate over SA. We present a leaf wax hydroclimate record from ODP 1084, in the BUS, which reveals that changes in the isotopic signature of precipitation over SA coincide with a strengthening of the MTG across the Mid-Pleistocene Transition (MPT). We use HadCM3 simulations to demonstrate the sensitivity of winter rainfall to shifts in the MTG during the MPT. Given the ongoing impacts of climate change on water resources in SA, awareness of the relationship between rainfall and shifts in Hadley Circulation could provide insight into past water availability and aid regional adaptation efforts.

The Mid-Pleistocene Transition (1.2–0.7 Ma, MPT) represents a time of planetary transition, from milder 40 thousand-year (kyr) glacial cycles to more extreme 100 kyr glacial cycles. The cause of this shift is debated, but appears to be linked to changes in the carbon cycle (see Herbert (2023) and the references therein). Several lines of evidence suggest that these climate changes may have perturbed the local ecologies of several regions, including Southern Africa. For example, isotopic measurements of faunal remains (e.g., grazer tooth enamel, ostrich egg shells) suggest dietary changes in grazers and increases in relative humidity around 0.9–0.8 Ma¹, which, paired with phytolith morphotype analyses from Wonderwerk Cave^{2,3} and sedimentological data from Mamatwan Mine⁴, suggests shifts in moisture availability during the MPT. However, the scarcity and coarseness of these records makes it difficult to ascertain whether this is a signal of local variability, a regional trend, or whether a moisture shift is part of an overarching climate regime change.

There are compelling reasons to think that the MPT would affect climate across Southern Africa (SA, Fig. 1a). One prominent hypothesis about the MPT climate shift posits that expanded sea ice near Antarctica strengthened Southern Ocean (SO) stratification and induced ocean circulation changes^{5–7}. This would impact global and regional climates, especially in SA, where the surrounding ocean is a confluence of the Benguela Upwelling System (BUS), the Agulhas System, and the Antarctic circumpolar frontal system (AFS). The intensity of the Agulhas Leakage (AL), warm and salty masses of water which escape the retroflection of the Agulhas Current, is hypothesized to be modulated by variations of the westerly wind belt and AFS⁸. Proxy records associate intervals of reduced AL with northward shifts of the AFS, which occurred over the MPT and during post-MPT glacial periods^{9–11}. Northward migrations of the AFS and diminished AL are linked to the intensification of winter rainfall over SA on millennial timescales^{12,13}, however, there is debate over precisely how the westerlies, AFS, and AL influence SA rainfall in the modern^{14–16}.

¹Department of Earth and Environmental Sciences, Syracuse University, Syracuse, NY, USA. ²School of Geographical Sciences, University of Bristol, Bristol, UK. ³State Key Laboratory of Tibetan Plateau Earth Systems, Environment and Resources, Institute of Tibetan Plateau Research, Chinese Academy of Sciences, Beijing, China. ⁴Department of Geography, Durham University, Lower Mountjoy, Durham, UK. ⁵School of Geography, Queen Mary University of London, London, UK. ⁶These authors contributed equally: Alexander Farnsworth, Paul Valdes, Erin L. McClymont, Heather Ford. ✉e-mail: crubbelk@syr.edu

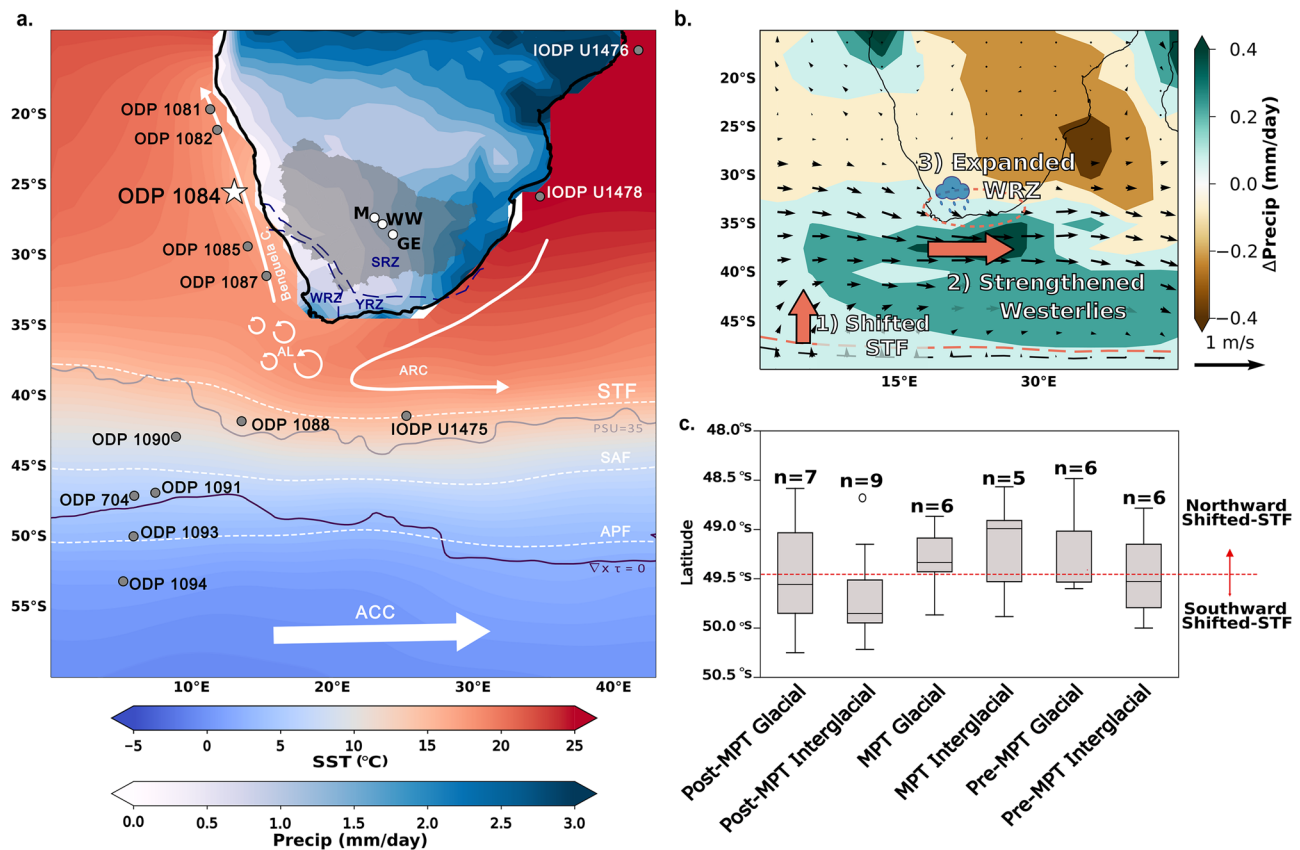


Fig. 1 | Regional climatology, site locations, and model results. **a** Modern climatology of the Southern Africa from reanalysis data. The Orange River watershed is mapped using HydroSHEDS data products⁹⁶. The white star marks the location of Ocean Drilling Program (ODP) Site 1084. Other ODP and International Ocean Discovery Program (IODP) drill sites discussed in the text are marked with gray circles; white circles mark the Mamatwan Mine (M), Wonderwerk Cave (WW), and Gharp Escarpment (GE) archaeological sites discussed in the text. Dashed blue contours over the land denote the extent of the winter, yearly, and summer rainfall zones (WRZ, YRZ, and SRZ, respectively). White arrows highlight the Benguela Current, Agulhas Leakage (AL), Agulhas Return Current (ARC), and Antarctic Circumpolar

Current (ACC). The dashed white contours mark the fronts within the Antarctic Frontal System (AFS): Subtropical Front (STF), Subantarctic Front (SAF), and Antarctic Polar Front (APF) based on isotherms^{93,94}. The gray contour marks the 35 PSI isohaline and the black contour marks the line of zero Windstress Curl (WSC). **b** Simulated annual average precipitation for model runs with a northerly placed line of zero WSC minus runs with a southerly placed line of zero WSC. **c** Simulated latitudinal position of the line of zero WSC for glaciials and interglaciials before, during, and after the Mid-Pleistocene Transition (MPT), demonstrating that the model produces a northerly displacement of the AFS during the MPT and glaciials. The number of models (n) used for each interval is noted.

A more robust understanding of the complex SA hydroclimate system is vital for assessing past and future changes in hydroclimate. Here, we demonstrate that substantial shifts in the leaf wax isotopic signatures of precipitation and vegetation over Southern Africa coincide with significant shifts in the position of the AFS across the MPT. We use HadCM3 simulations to test for a regionally coherent mechanism which reconciles the different perspectives gained from the terrestrial versus marine records (e.g., assess whether a shift in hydroclimate related to large-scale circulation shifts). In particular, we test the hypothesis that northward shifts in the AFS resulted in an expansion of the winter rainfall zone (WRZ) and WRZ-type vegetation (i.e., C₃ plants) from 1.5 to 0.9 Ma, and that a sudden withdrawal of the AFS after 0.9 Ma prompted a contraction of WRZ rainfall and vegetation. We conclude by discussing the parallels between the mechanism presented here and that which drove extreme drought in SA in recent years; we raise the question of whether the relatively short-lived, but intense, drought events we see in the modern have the potential to become longer-lived features of the future climatology.

Results and discussion

Leaf-Wax analysis of sediment from ODP 1084

ODP 1084 (25° 30.8345'S, 13° 01.6668'E) is located in the central upwelling cell of the BUS (Fig. 1a); age control is derived from shipboard magnetostratigraphy and nannofossil datums¹⁷. Terrigenous

materials are transported to marine sediments via aeolian processes¹⁸ and fluvial transport from the Orange River watershed¹⁹. Sediments from the watershed enter the water column at the Orange River delta, approximately 250 km south of ODP 1084; a portion of this sediment is carried northward to ODP 1084 via the Benguela Current²⁰ while the rest is transported southward via a coastal counter current²¹. The large source area for ODP 1084 means that contributions from a variety of biomes, including the Succulent Karoo, Nama Karoo, Kalahari Savannah, and grasslands, are integrated into a single signal, which ultimately represents regional trends, rather than localized variability.

Paired carbon and hydrogen isotopic analyses of plant leaf waxes are commonly used to infer the relative proportions of C₃ to C₄ vegetation and the hydrogen isotopic signature of precipitation, respectively, especially in Africa (e.g., Feakins et al.²²; Tierney et al.²³; Lupien et al.²⁴). Such methodology is appropriate for regions with little or no presence of CAM vegetation, but may not work well in Southwestern Africa, where CAM plants are more prominent^{25,26}; the broad range of $\delta^{13}C_{wax}$ values that CAM plants display make them impossible to differentiate from C₃ and C₄ using $\delta^{13}C_{wax}$ alone²⁷. Furthermore, there is high uncertainty regarding the apparent fractionation of hydrogen in CAM plants, which is well constrained for C₃ and C₄ vegetation. To examine the impact of overlooking the potential influence of CAM plants on δD_{wax} , we performed a carbon-correction using a standard methodology to infer the hydrogen isotopic signature of

precipitation (see Methods for details) and found that the correction artificially smooths the δD_p record (Fig. S5). As such, we utilize the raw, uncorrected δD_{wax} data in our statistical analyses.

While we cannot reliably use $\delta^{13}C_{wax}$ on its own to estimate vegetation changes in this region, we may be able to characterize overall biome transitions by leveraging the ratios between individual *n*-alkanes. Empirical studies have demonstrated that the ratios between individual *n*-alkanes are sensitive to environmental changes (e.g., ref. 28), and biomes in Southwestern Africa can be characterized by these ratios²⁹. We use ratios of different *n*-alkanes (e.g., Norm31 and Norm33) to roughly track the contribution of the WRZ taxa to our record because these metrics reflect the relative wax contribution of different biomes to the sediment (see methods for more details). Finally, we use simulations from the Hadley Centre Coupled Model 3 (HadCM3) to examine the dynamics driving changes in δD_{wax} . Despite modifications aimed toward more accurately capturing the meridional temperature gradient (MTG)³⁰, HadCM3 remains particularly biased toward warmth over parts of the SO and BUS. Comparing the Pre-industrial control run to observational data (Fig. S2), we find the model simulates a weaker temperature gradient over the AFS and weaker westerlies than those observed in the modern. Considering this bias, along with the limitations of a low spatial resolution, we use the model to examine the sensitivity of rainfall to changes in the AFS, rather than treating the model output as an exact picture of MPT climate (see Methods for further analytical and model details). Given the more southerly placement of the SO boundary in the model, we expect rainfall responses to be similarly displaced.

Coordinated changes in Southern African hydroclimate during the MPT

Lomb-Scargle (LS) periodogram analysis on δD_{wax} (Fig. S6) indicates possible low-frequency orbital influence in the 400-kyr and 100-kyr bands from 0.8 Ma to present, though confidence is low (less than 75%). Given the prominence of orbital signals in other African hydroclimate records (e.g., refs. 31–33, the lack of orbital variability in our record is probably due to low sampling resolution (>21-kyr between many samples, Fig. S1). Rather than orbital-scale variability, we observe broad trends in the δD_{wax} and $\delta^{13}C_{wax}$ records over the past 3.4 Ma (Fig. 2a, b). We also observe relatively abrupt enrichment in both δD_{wax} and $\delta^{13}C_{wax}$ records over the MPT, particularly at -0.85–0.75 Ma.

The overarching trends in δD_{wax} and $\delta^{13}C_{wax}$ are likely related to long-term changes in both regional and global SSTs. Varimax factor analysis (see Methods for details) of our records and several regional proxy records (Fig. 3) identifies two primary modes of variability which explain ~60% of the variance in the data. The first mode (Factor 1; Fig. 3a, c), which explains 42.62% of the variance, captures the long-term trends in BUS temperatures, hydroclimate, and vegetation, and dust accumulation; Factor 1 thus links the intensification of the BUS to the overall aridification of the African continent^{34,35}. The secondary mode of variability (Factor 2; Fig. 3b, d) explains 20.56% of the variance in the data and indicates that changes in the MTG are strongly tied to changes in the nutrient availability within the BUS (ODP 1084 Alkenone MAR) and relatively abrupt variations in δD_{wax} . The abrupt enrichment in δD_{wax} around -0.9–0.75 Ma is thus likely influenced by similarly stark changes in ocean conditions. The changes in $\delta^{13}C_{wax}$ are probably tied to changing hydroclimate, though $\delta^{13}C_{wax}$ loads less strongly on Factor 2.

Due to its stratiform character and relatively depleted vapor source (the South Atlantic), precipitation in the WRZ is depleted in deuterium relative that of the summer rainfall zone (SRZ), which is generally convective and utilizes a relatively enriched vapor source (the Indian Ocean)^{36–38}. An isotopic gradient exist within the SRZ, as precipitation moves inland from the coast and undergoes fractionation by both the amount and continental effects^{29,36,38,39}; due to its smaller spatial extent and lower overall precipitation volume, the

isotopic signature of rainfall in the WRZ is less impacted by these effects^{38,40}. The vegetation of each rainfall zone is distinct: the Fynbos, Succulent and Nama Karoo biomes (mainly *C*₃ and CAM plants) dominate in the WRZ, while grassland and savannah (mostly *C*₄ plants) are more prevalent in the SRZ²⁶. Norm31-Norm33 approaches zero at -0.9 Ma, which may indicate an increased contribution of waxes from grassland and savannah biomes (Fig. S7). We therefore interpret the abrupt enrichment of the ODP 1084 δD_{wax} and $\delta^{13}C_{wax}$ signals as contraction of the winter rainfall zone and associated vegetation types from -0.9–0.75 Ma. This interpretation is consistent with multiple terrestrial records from the Kalahari which indicate a substantial hydroclimate and vegetation shift occurred around 0.9–0.8 Ma¹⁴¹.

Antarctic front migration mechanism

Assessment of regional proxy records presents a compelling mechanism for this shift in seasonality. Around 1.5 Ma, Southern Hemisphere extratropical temperatures cooled rapidly, falling below preindustrial levels (Fig. S7^{42,43}). This cooling resulted in a strengthening of the MTG (Figs. 2h, S6) and allowed for an expansion of sea ice (Fig. 2m⁷), which prompted a reorganization of ocean circulation^{6,7,44,45}. In the surface waters, a steeper temperature gradient over the SO shifted the AFS northward; the presence of foraminifera generally found in Antarctic and sub-Antarctic waters (e.g., refs. 11,46,47), along with records of opal deposition^{48–50} and primary productivity^{11,51}, indicate a more northerly presence of the AFS prior to ~1 Ma. The northward presence of the AFS may have also created a choke-point at the Agulhas Plateau which limited AL (Fig. 2l¹⁰), and, combined with lower sea levels and weakened Indonesian Throughflow, caused a build-up of warmer, saline waters in the western Indian Ocean (Fig. 2k⁵²). The strengthened MTG, expansion of sea ice, and limited AL probably impacted deep water circulation as well: foraminiferal trace elements and authigenic Nd isotope proxies indicate increased carbon storage and weaker Atlantic Meridional Overturning Circulation over the MPT, culminating in a meridional overturning minimum at -0.9 Ma^{6,44}.

Changes of the MTG influence the width (and intensity) of atmospheric Hadley circulation, with models and modern observations demonstrating that a weaker gradient drives an expansion of the Hadley cell^{53,54} and a poleward propagation of the westerly storm track^{53,55–58}. By this same mechanism, a steepening of the MTG from -1.5 to 1.1 Ma and from -1 to 0.8 would cause a contraction of the Hadley cell and an equatorward propagation of the westerly storm track. As winter storms travel further north, the WRZ would expand and the proportion of winter to summer rain would increase; an increase in isotopically depleted winter rains would contribute to the gradual depletion of deuterium in δD_{wax} prior to 0.9 Ma³⁸.

As mentioned previously, the model's resolution limitations and temperature bias result in a more poleward-displaced SO position in PI simulations compared to observations, and any rainfall response to changes in the SO is expected to be similarly displaced. The HadCM3 simulations feature northward shifts of the subtropical front and a strengthening of the southern westerlies which result in both a zonal increase and intensification of winter rainfall over the waters south of Africa and parts of SA during the MPT (Fig. 1b, c). The model results thus demonstrate the sensitivity of winter rainfall to dynamical changes in the westerlies and SO. Further work examining this response in models of higher resolution and with the ability to trace water isotopologues is needed.

Frontal system retreat

From -1.1 to 1 Ma and -0.8–0.75 Ma, the Southern Hemisphere MTG rapidly weakened (Figs. 2h, S7). The first weakening, from -1.1 to 1 Ma, occurred as tropical SSTs rapidly decreased, is probably due to an increase of equatorial upwelling as the Hadley Circulation intensified^{59–61}. Despite a weaker MTG, the proxy evidence indicates that the AFS remained in a northerly position from -1.1 to 1 Ma.

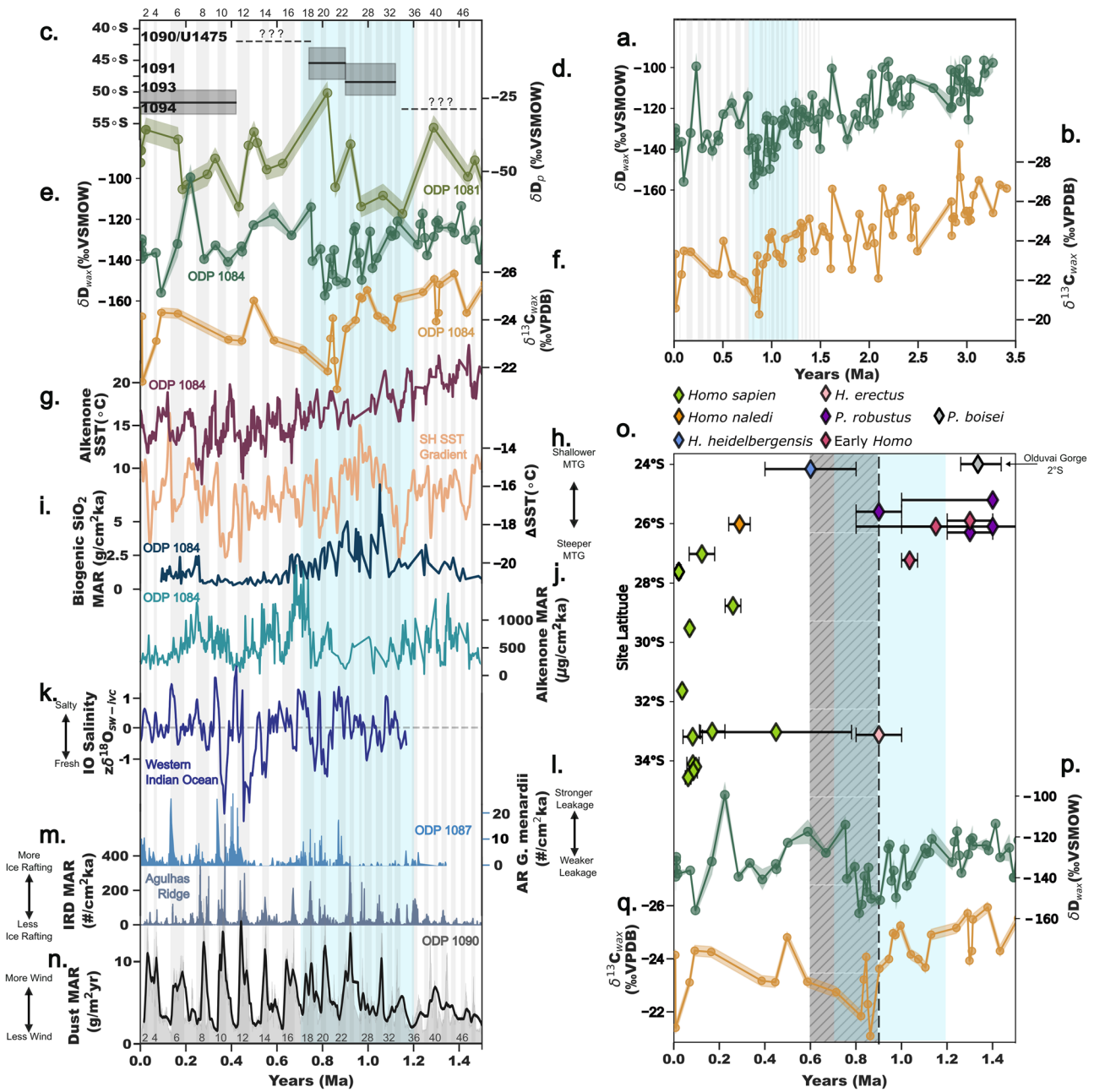


Fig. 2 | A compilation of proxy records. Top Right: The full Plio-Pleistocene **a** δD_{wax} and **b** $\delta^{13}C_{wax}$ records for Ocean Drilling Program (ODP) Site 1084, error bars indicate $\pm 1\sigma$. Vertical gray bars in both the Top Right and Left panels indicate glacial intervals; the vertical blue bar in each panel highlights the Mid-Pleistocene Transition. Left: A compilation of records from the last 1.5 Ma. **c** gray bars indicate the latitudinal position the Antarctic Polar Front (and the circumpolar biogenic opal belt) based on the presence of laminated diatom mats (i.e., biogenic opal deposits), dashed lines indicate estimated position of the front⁵⁰; **d** the ODP 1081 δD_p record⁶²; **e, f** are the last 1.5 Ma of (**a, b**), respectively; **g** alkenone based sea

surface temperatures (SST) records from ODP 1084⁶¹, **h** Southern Hemisphere SST gradient (extratropical - tropical Atlantic, see Fig. S7 for details); **i** biogenic SiO_2 mass accumulation rates (MAR) from ODP 1084¹⁷; **j** alkenone MAR from ODP 1084⁶¹; **k** Indian Ocean salinity record⁵²; **l** *G. menardii* accumulation rate¹⁰; **m** ice rafted debris records from the Agulhas Ridge⁷; **n** the dust MAR record from ODP 1090⁵⁹. Bottom Right: **o** scatter plot displaying the compiled locations and dates of Southern African hominin fossils or ages of the beds containing said remains (see Data Availability Statement), the hatched bar highlights a relative gap in the fossil record; **p, q** are the same as (**a, b**), respectively.

From -0.8 to 0.75 Ma, SSTs in both the tropics and Southern Hemisphere Atlantic extratropics increased - the weakening of the MTG appears to have been driven by differences in the rates of warming, as the extratropics appear to have warmed more rapidly than the tropics (Fig. S7). During this interval, sea ice retreated⁷ and AL resumed¹⁰. The coincident decrease and increase in the respective accumulation rates of biogenic silica and alkenones at ODP 1084 suggests the withdrawal of polar nutrients from the BUS^{17,49,60} as the AFS retreated.

As the AFS and winter storm track migrated southward, the extent of the WRZ would be limited; the abrupt enrichment in δD_{wax} at ODP 1084 and ODP 1081⁶² is consistent with an increase in the proportion of summer rainfall³⁸. The stark fluctuation in $\delta^{13}C_{wax}$ values over this interval indicate a vegetation shift over the leaf wax source area, and our inference that wax contribution from grassland and savannah biomes increased at -0.8 Ma is consistent with an expansion of the SRZ. Improved sampling resolution during the Late Pleistocene is

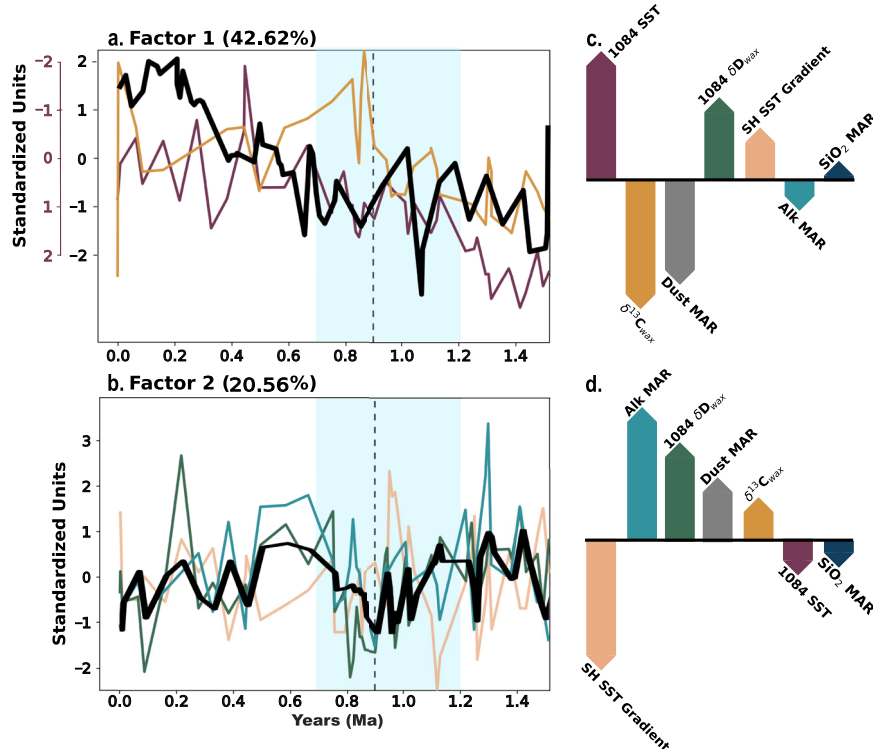


Fig. 3 | Varimax factor analysis of leaf wax isotopes, BUS sea surface temperatures (SST) and productivity proxies, and Southern Ocean dust flux. **a** Timeseries of Factor 1 (black) plotted against the standardized timeseries of the variables with the strongest loadings (ODP 1084 SST and $\delta^{13}C_{wax}$). **b** Timeseries of Factor 2 (black) plotted against the standardized timeseries of the variables with

the strongest loadings (Southern Hemisphere (SH) SST gradient, alkenone mass accumulation rate (MAR), and 1084 δD_{wax}). **c, d** Bar plots rank the relative loading of variables on each factor, where the leftmost bar indicates the largest loading and the rightmost bar indicates the smallest loading. Note units are arbitrary and colors match those of the corresponding variable in Fig. 2.

needed to further examine the impacts of glacial/interglacial variability on δD_{wax} and $\delta^{13}C_{wax}$ after the MPT.

Comparison to terrestrial and tropical records

The interpretation of the ODP 1084 leaf wax records presented here agrees with multiple terrestrial records from the Kalahari which indicate a substantial hydroclimate shift occurred around 0.9–0.8 Ma^{1,4,41,63}. For example, sedimentological evidence from Mamatwan Mine, -1000 km inland from ODP 1084, points to the presence of a shallow water body from -1.5 to 1 Ma^{4,63}. The remains from lechwe antelope (*Kobus lechwe*), which require standing bodies of water, have been found at Wonderwerk Cave¹ and regions of the Ghaap Escarpment⁶⁴, indicating that similar shallow water bodies were present throughout the southern Kalahari during this interval. Just as the extension of the WRZ, and adjacent yearly rainfall zone, would help sustain these shallow waters, the contraction of these zones could help explain their disappearance after 0.9 Ma.

The mechanism presented here also supports tropical vegetation reconstructions for the MPT. Leaf wax records from ODP 1077, near the equator, indicate an increase (decrease) in tropical savannah (C_3 rainforest taxa) in the Congo Basin from -0.95–0.85 Ma, and a reverse of this trend after -0.85 Ma, which the authors link to tropical SSTs⁶⁵. East African soil carbonates demonstrate large inter-site variability; most sites in East Africa display a broad trend toward tropical C_4 savannah over the last -4 Ma, however, the records from several locations feature substantial C_3 incursions (e.g., Maslin et al.⁶⁶, Lüdecke⁶⁷, Quinn et al.⁶⁸). The shifting MTG and Hadley circulation would have impacted the placement of the Intertropical Convergence Zone, water availability, and subsequent ecosystems variation in the tropics.

Implications for hominin evolution

Elucidation of past hydroclimate change may be useful to contextualize hominin evolution in SA. Hominin individuals living in this region would have experienced abrupt, but extensive landscape change alongside dwindling freshwater resources and a coincident vegetation shift. At the same time, there is a relative reduction in artifact densities in the corresponding strata of Wonderwerk Cave^{2,69}, as well as the last appearance of *Paranthropus boisei* in the SA archaeological record (e.g., Herries 2022). However, more rigorous work examining the impact of precipitation and landscape change on *Paranthropus* is necessary.

Implications for future climate

A deeper understanding of the mechanism presented in this study is vital for understanding and predicting modern and future climate events. From 2015 to 2018, the Day-Zero Drought devastated water supplies across southwestern Africa^{70–72}. Intense scrutiny of this drought has pointed to an expansion of the Hadley cell and subsequent poleward displacement of the mid-latitude westerlies as the primary driver^{57,73–75}. At the synoptic scale, the Hadley expansion may be increasing the frequency of South Atlantic Anticyclone ridging high-pressure systems^{57,75,76}, ultimately resulting in a delayed and shortened wet-season^{75,76}. Outside of SA, the response of other Mediterranean-type climates to changes in Hadley circulation is varied and subject to regionally specific drivers⁷⁷. Compilation of hydrogen isotopic records of precipitation from Chile and South Australia (the other Southern Hemisphere Mediterranean-type climate zones) are thus needed to interrogate the local hydroclimate response to changes of the Hadley circulation and AFS over both modern and paleo-timescales.

The results presented in this paper bolster the view that long-term shifts in the Southern Hemisphere storm tracks may ultimately be

responsible for hydroclimate shifts in SA. Given the similarities of these past mechanisms to those observed in the modern, further work is needed to examine whether the relatively short-lived drought events we see in the modern have the potential to become longer-lived features of the future climatology. While we cannot prevent the next extreme drought from occurring, an enhanced understanding of the underlying mechanics of regional hydroclimate may provide additional insight which improves our projections of regional climate, aids mitigation efforts, and strengthens the resilience of SA communities to the effects of anthropogenic climate change.

Summary

This study highlights substantial shifts in rainfall seasonality and vegetation cover which are associated with migrations of the AFS over the MPT. We use HadCM3 simulations to further demonstrate that SA precipitation is sensitive to variations in the westerlies and AFS; this work would benefit from additional analyses using isotope-enabled simulations with higher spatial resolution. Our records supplement the existing terrestrial records of hydroclimate change in SA. We present a mechanism of hydroclimate change during the MPT which is analogous to that of the Day-Zero Drought, suggesting that these impactful drought events we see in the modern record have the potential to become persistent features of the region's climatology. Continued investigation of this mechanism in the past and present is therefore needed to improve our projections of, and preparations for, future extreme climate events.

Methods

Sample preparation and analytical methods

Samples were freeze-dried and homogenized, and total lipids (TLEs) were extracted and purified via column chromatography. Concentrations of C₂₉ and C₃₁ alkanes were quantified using a Trace 1310 GC-FID, and their hydrogen and carbon isotopic compositions were measured using a Thermo Scientific Trace 1310 GC and a PTV injector connected via an IsoLink II pyrolysis furnace to a Delta V Plus isotope ratio mass spectrometer (GC-IRMS). H₂ and CO₂ gases calibrated to an *n*-alkane standard (A7 mix provided by Arndt Schimmelmann at Indiana University) provided references for each analysis and were used to monitor drift. H₃ factor measured daily over the course of the hydrogen analyses averaged 4.703 ppm/V over a range of 1–8 V. Samples were run in triplicate for δD to obtain a precision better than 3‰ (1- σ), and duplicate or triplicate for $\delta^{13}C$ to obtain a precision better than 0.2‰ (1- σ).

We calculated a mean carbon preference index >1, indicating terrestrial rather than petrogenic inputs⁷⁸, and an mean average chain length (ACL) of 29.35 ± 0.089 (1- σ). Because concentrations of the C₂₉ and C₃₁ alkanes were similar (within 2.5 ng/g of one another), and because previous studies from SWA have focused on the C₃₁ alkane as a proxy for precipitation (e.g., refs. 35,62), we report isotopic results from this chain length.

Inferring δD of precipitation from leaf waxes

The carbon isotopic measurements of 70 samples were paired with 106 hydrogen isotopic measurements of the C₃₁ alkane ($\delta^{13}C_{wax}$ and δD_{wax} , respectively) to infer the hydrogen isotopic signature of precipitation, δD_p . δD_{wax} is offset from the hydrogen isotopic signature of the environmental source waters, generally assumed to be precipitation; this apparent fractionation, ϵ_{p-w} , varies systematically across plant clades^{79,80}, with graminoids generally having a larger ϵ_{p-w} than those of eudicots^{79,81}.

Within a Bayesian framework, we use $\delta^{13}C_{wax}$ and empirically derived constraints on ϵ_{p-w} from modern grasses and eudicots (Table S1²³), to infer the proportion of graminoids in our sample and weigh our ϵ_{p-w} accordingly. The resulting ϵ_{p-w} accounts for the variable

fractionation between graminoids and eudicots (Eq. 1).

$$\epsilon = (f_{C4}) \cdot \epsilon_{C4} + (1 - f_{C4}) \cdot \epsilon_{C3} \quad (1)$$

We then use our weighted ϵ_{p-w} to infer δD_p (Eq. 2).

$$\delta D(\text{precip}) = \frac{1000 + \delta D_{wax}}{(\epsilon/1000) + 1} - 1000 \quad (2)$$

This approach has been widely applied to infer δD_p from leaf wax δD_{wax} in a variety of paleoclimatic studies (e.g., Tierney et al.²³, Bhat-tacharya et al.⁸², Windler et al.⁸³).

n-Alkane ratio calculation

Herrmann et al.²⁹ measured *n*-alkanes in soils, sediments, and river deposits from several biomes across Southern Africa and calculated the ratio of *n*-alkane homologues C₂₉ and C₃₁ and C₂₉ and C₃₃ as

$$\text{Norm31} = C_{31}/(C_{29} + C_{31}) \quad (3)$$

and

$$\text{Norm33} = C_{33}/(C_{29} + C_{33}) \quad (4)$$

where C_x is the concentration of the *n*-alkane with x carbon atoms.

Their results showed that in samples from the Grassland and Savannah biomes (which are mainly SRZ flora), Norm31 ≈ Norm33, but for samples from the Fynbos, Succulent Karoo, and Nama Karoo biomes (primarily in the WRZ), Norm31 > Norm33.

Based on their results, we tentatively infer the relative contributions of SRZ flora vs WRZ flora by taking the difference of Norm31 and Norm33. If Norm31-Norm33 ≈ 0, we infer that wax contributions mostly came from the Grassland or Savannah biomes. If Norm31-Norm33 > 0, we infer that wax contributions include more contributions from the Fynbos, Succulent, or Nama Karoo biomes.

Using this index, we infer more contribution from the Fynbos, Succulent Karoo, and/or Nama Karoo biomes 1.5–1 Ma, and decreasing contribution from these biomes after 1 Ma. The agreement of this inference with evidence of vegetation changes from the Kalahari interior (e.g., phytolith morphotpe analyses^{2,3}, dietary changes in grazers¹), lends credence to this index. Further work needs to be done to examine whether this index is viable outside of southwestern Africa.

Varimax factor analysis

Varimax Factor Analysis (VFA) is a type of matrix decomposition similar to Principal Component Analysis (PCA); the goal of both techniques is to reduce the number of variables while retaining as much of the original information as possible^{84,85}. However, VFA assumes there is an unobserved variable (or latent factor) which exerts a causal influence upon the observed variables⁸⁵ -this assumption ultimately allows for a more simple interpretation of the underlying structure of the correlations between measured variables.

We performed this analysis using the scikit-learn python toolkit⁸⁶. The dataset was first standardized and normalized using the scikit-learn pre-processing tools, then the VFA was performed using the appropriate functions from the scikit-learn decomposition module. The results are listed in Table S2.

Model description and results

We utilize a suite of simulations from the Hadley Centre Coupled Model 3 (HadCM3). HadCM3 is a coupled climate model comprised of a 3-dimensional dynamical atmosphere component with a resolution of 2.5° × 3.75° and 19 vertical levels, and an ocean model with a resolution of 1.25° × 1.25° and 20 vertical levels (see Valdes et al.⁸⁷ for a

detailed overview). These simulations cover the last 3.6 Ma and were run every 4 ka using a configuration of HadCM3 which includes a tiling of surface types within MOSES2.1 d⁸⁸ and additional atmospheric and vegetation moisture stress parameterizations to better simulate a ‘Green Sahara’ during the mid-Holocene⁸⁹. The model also includes several parameterizations to better resolve the ‘Cold-Pole Paradox’³⁰: major parameterizations include modified cloud condensation nuclei density and cloud droplet effective radius, which better aligned the simulated meridional temperature gradient with proxy observations; adjustments to the ocean model to removed nonlinear instabilities; and the addition of sea ice, which was calculated on a zero-layer model and allowed for partial sea-ice coverage.

Despite these modifications, HadCM3 remains particularly biased toward warmth over parts of the Southern Ocean - comparison to COBE SST data⁹⁰ demonstrates that HadCM3 simulates a substantially weaker temperature gradient over the AFS. Considering this bias, along with the limitations of a low spatial resolution, we use the model to examine whether a northward shift of the Southern Ocean is simulated during the MPT and whether this northward movement is associated with any change in the WRZ, rather than treating the model output as an exact picture of MPT climate.

We select 39 simulations from six categories: Pre-MPT Interglacials and Pre-MPT Glacials, MPT Interglacials and MPT Glacials, and Post-MPT Interglacials and Post-MPT Glacials. Each category is comprised of select model runs from within the specified interval and a complete list of these simulations can be found in Table S3.

We assess whether the selected model simulations capture shifts in SA precipitation that are consistent with δD_p across the MPT. We focus on zonal winds and precipitation, and we use the line of zero WSC (WSC = 0)^{91,92} as indicator of the northern edge of the AFS (i.e., the STF). We considered using the position of the 11degC isotherm as a marker of the AFS^{91,93,94}), however Southern Ocean temperature biases in the model⁸⁷ mean the isotherm may not actually correspond to the location of the front.

The average latitudinal position of WSC = 0 across all model runs is 49.48°S - any model run with a WSC = 0 placement north of 49.48°S was classified as northward-shifted and those with a WSC = 0 placement south of 49.48°S was considered southward-shifted (Fig. 1b). Most Pre- and Post-MPT glacial runs were classified as northward-shifted, as are most MPT glacial and interglacial runs. Pre- and Post-MPT interglacial runs were largely categorized as southward-shifted.

To evaluate the dynamical and hydroclimate responses to simulated shifts in the STF, we subtract the average precipitation and wind fields of the southward-shifted models from the northward-shifted models (Fig. 1c). As expected, the westerly wind belt is shifted northward and strengthened in northward-shifted runs. These model runs simulate less terrestrial rainfall than the southward-shifted runs, particularly over the SRZ. However, the WRZ does expand zonally and experiences a slight increase in rainfall, and precipitation south of Africa increases substantially.

Data availability

The ODP 1084 leaf wax data generated in this study are available on the NOAA/NCCEI Paleoclimatology Database at <https://www.nccei.noaa.gov/access/paleo-search/study/41028>. Model data is available after user registration at <https://www.paleo.bristol.ac.uk> under the ‘Model Output’ tab⁸⁷. All previously published data is available in the respective publications. Data from Fig. 2o was sourced from⁹⁵ and the references therein.

References

- Ecker, M. et al. The palaeoecological context of the Oldowan-Acheulean in southern Africa. *Nat. Ecol. Evol.* **2**, 1080–1086 (2018).
- Chazan, M. et al. The Oldowan horizon in Wonderwerk Cave (South Africa): archaeological, geological, paleontological and paleoclimatic evidence. *J. Hum. Evol.* **63**, 859–866 (2012).
- Rossouw, L. An early pleistocene phytolith record from wonderwerk Cave, Northern Cape, South Africa. *Afr. Archaeol. Rev.* **33**, 251–263 (2016).
- Vainer, S., Erel, Y. & Matmon, A. Provenance and depositional environments of Quaternary sediments in the southern Kalahari Basin. *Chem. Geol.* **476**, 352–369 (2018).
- Lear, C. H. et al. Breathing more deeply: deep ocean carbon storage during the mid-Pleistocene climate transition. *Geology* **44**, 1035–1038 (2016).
- Farmer, J. R. et al. Deep Atlantic Ocean carbon storage and the rise of 100,000-year glacial cycles. *Nat. Geosci.* **12**, 355–360 (2019).
- Starr, A. et al. Antarctic icebergs reorganize ocean circulation during Pleistocene glacials. *Nature* **589**, 236–241 (2021).
- Bard, E. & Rickaby, R. E. Migration of the subtropical front as a modulator of glacial climate. *Nature* **460**, 380–383 (2009).
- Peeters, F. J. et al. Vigorous exchange between the Indian and Atlantic oceans at the end of the past five glacial periods. *Nature* **430**, 661–665 (2004).
- Caley, T., Giraudeau, J., Malaizé, B., Rossignol, L. & Pierre, C. Agulhas leakage as a key process in the modes of Quaternary climate changes. *Proc. Natl. Acad. Sci. USA* **109**, 6835–6839 (2012).
- Nirmal, B. et al. Agulhas leakage extension and its influences on South Atlantic surface water hydrography during the Pleistocene. *Palaeogeogr. Palaeoclimatol. Palaeoecol.* **615**, 111447 (2023).
- Stuut, J. B. W., Crosta, X., Borg, K. & Schneider, R. Relationship between Antarctic sea ice and southwest African climate during the late Quaternary. *Geology* **32**, 909–912 (2004).
- Weldeab, S., Stuut, J. B. W., Schneider, R. R. & Siebel, W. Holocene climate variability in the winter rainfall zone of South Africa. *Climate* **9**, 2347–2364 (2013).
- Beal, L. M., De Ruijter, W. P., Biastoch, A. & Zahn, R. On the role of the Agulhas system in ocean circulation and climate. *Nature* **472**, 429–436 (2011).
- Cheng, Y., Beal, L. M., Kirtman, B. P. & Putrasahan, D. Interannual Agulhas leakage variability and its regional climate imprints. *J. Clim.* **31**, 10105–10121 (2018).
- Tim, N., Zorita, E., Hünicke, B. & Ivanciu, I. The impact of the Agulhas current system on precipitation in southern Africa in regional climate simulations covering the recent past and future. *Weather Clim. Dyn.* **4**, 381–397 (2023).
- Lange, C. B., Berger, W. H., Lin, H. L. & Wefer, G. The early Matuyama Diatom Maximum off SW Africa, Benguela Current System (ODP Leg 175). *Mar. Geol.* **161**, 93–114 (1999).
- Dupont, L. M. & Wyputta, U. Reconstructing pathways of aeolian pollen transport to the marine sediments along the coastline of SW Africa. *Quat. Sci. Rev.* **22**, 157–174 (2003).
- Vogts, A., Schefuß, E., Badewien, T. & Rullkötter, J. n-Alkane parameters from a deep sea sediment transect off southwest Africa reflect continental vegetation and climate conditions. *Org. Geochem.* **47**, 109–119 (2012).
- Bluck, B. J., Ward, J. D., Cartwright, J. & Swart, R. The Orange River, southern Africa: an extreme example of a wave-dominated sediment dispersal system in the South Atlantic Ocean. *J. Geol. Soc.* **164**, 341–351 (2007).
- Rogers, J. & Bremner, J. The Benguela ecosystem. Part VII. Marine-geological aspects. *Oceanogr. Mar. Biol. Ann. Rev.* **29**, 1–85 (1991).
- Feakins, S. J., Peter, B. & Eglinton, T. I. Biomarker records of late Neogene changes in northeast African vegetation (12), 977–980 <https://doi.org/10.1130/G21814.1> (2005).
- Tierney, J. E., Pausata, F. S. R. & De Menocal, P. B. Rainfall regimes of the Green Sahara. *Sci. Adv.* **3**, 1–10 (2017).

24. Lupien, R. et al. Low-frequency orbital variations controlled climatic and environmental cycles, amplitudes, and trends in northeast Africa during the Plio-Pleistocene. *Commun. Earth Environ.* **4** <https://doi.org/10.1038/s43247-023-01034-7> (2023).
25. Rutherford, M. C., Mucina, L. & Powrie, L. W. "Biomes and bioregions of southern Africa." In *The vegetation of South Africa, Lesotho and Swaziland* Vol 19 30–51 (2006).
26. Mucina, L., Rutherford, M. C. & Powrie, L. W. "Vegetation Atlas of South Africa, Lesotho and Swaziland." In *The vegetation of South Africa, Lesotho and Swaziland* 748–789 (2006).
27. Boom, A., Carr, A. S., Chase, B. M., Grimes, H. L. & Meadows, M. E. Leaf wax n-alkanes and $\delta^{13}C$ values of CAM plants from arid southwest Africa. *Org. Geochem.* **67**, 99–102 (2014).
28. Carr, A. S. et al. Leaf wax n-alkane distributions in arid zone South African flora: environmental controls, chemotaxonomy and palaeoecological implications. *Org. Geochem.* **67**, 72–84 (2014).
29. Herrmann, N. et al. Sources, transport and deposition of terrestrial organic material: a case study from southwestern Africa. *Quat. Sci. Rev.* **149**, 215–229 (2016).
30. Fenton, I. S., Aze, T., Farnsworth, A., Valdes, P. & Saupe, E. E. Origination of the modern-style diversity gradient 15 million years ago. *Nature* **614**, 708–712 (2023).
31. Schefuß, E., Damsté, J. S. S. & Jansen, J. H. F. Forcing of tropical Atlantic sea surface temperatures during the mid-Pleistocene transition. *Paleoceanography* **19**, 1–12 (2004).
32. Dupont, L. Orbital scale vegetation change in Africa. <https://doi.org/10.1016/j.quascirev.2011.09.019>(2011).
33. Lupien, R. L. et al. Orbital controls on eastern African hydroclimate in the Pleistocene. *Sci. Rep.* **12**, 3170 (2022).
34. Hoetzel, S., Dupont, L., Schefuß, E., Rommerskirchen, F. & Wefer, G. The role of fire in Miocene to Pliocene C 4 grassland and ecosystem evolution. *Nat. Geosci.* **6**, 1027–1030 (2013).
35. Dupont, L. M., Rommerskirchen, F., Mollenhauer, G. & Schefuß, E. Miocene to Pliocene changes in South African hydrology and vegetation in relation to the expansion of C 4 plants. *Earth Planet. Sci. Lett.* <https://doi.org/10.1016/j.epsl.2013.06.005> (2013).
36. Dansgaard, W. Stable isotopes in precipitation. *Tellus* **16**, 436–468 (1964).
37. Aggarwal, P. K. et al. Proportions of convective and stratiform precipitation revealed in water isotope ratios <https://doi.org/10.1038/NNGEO2739> (2016).
38. Braun, K., Bar-Matthews, M., Ayalon, A., Zilberman, T. & Matthews, A. Rainfall isotopic variability at the intersection between winter and summer rainfall regimes in Coastal South Africa (Mossel bay, Western Cape Province). *South Afr. J. Geol.* **120**, 323–340 (2017).
39. Herrmann, N. et al. Hydrogen isotope fractionation of leaf wax n-alkanes in southern African soils. *Org. Geochem.* **109**, 1–13 (2017).
40. Harris, C., Burgers, C., Miller, J. & Rawoof, F. O- and H-isotope record of Cape Town rainfall from 1996 to 2008, and its application to recharge studies of table mountain groundwater, South Africa. *South Afr. J. Geol.* **113**, 33–56 (2010).
41. Lukich, V. & Ecker, M. Pleistocene environments in the southern kalahari of south africa. *Quat. Int.* **614**, 50–58 (2022).
42. McClymont, E. L., Sostdian, S. M., Rosell-Mel' e, A. & Rosenthal, Y. Pleistocene sea- surface temperature evolution: early cooling, delayed glacial intensification, and implications for the mid-pleistocene climate transition. *Earth Sci. Rev.* **123**, 173–193 (2013).
43. Clark, P. U., Shakun, J. D., Rosenthal, Y., Köhler, P. & Bartlein, P. J. Global and regional temperature change over the past 4.5 million years. <https://www.science.org> (2024).
44. Pena, L. D. & Goldstein, S. L. Thermohaline circulation crisis and impacts during the mid-Pleistocene transition. *Science* **345**, 318–322 (2014).
45. Starr, A. et al. Shift- ing Antarctic circumpolar current south of Africa over the past 1. 9 million years. *Sci. Adv.* **1692**, 1–10 (2025). (January).
46. Nirmal, B. et al. Pleistocene surface-ocean changes across the Southern subtropical front recorded by cryptic species of *Orbulina universa*. *Marine Micropaleontol.* **168** <https://doi.org/10.1016/j.marmicro.2021.102056> (2016).
47. Mohanty, R. N., Clemens, S. C. & Gupta, A. K. Dynamic shifts in the southern Benguela upwelling system since the latest Miocene. *Earth Planet. Sci. Lett.* **637**, 118729 (2024).
48. Cortese, G., Gersonde, R., Hillenbrand, C. D. & Kuhn, G. Opal sedimentation shifts in the World Ocean over the last 15 Myr. *Earth Planet. Sci. Lett.* **224**, 509–527 (2004).
49. Etourneau, J., Martinez, P., Blanz, T. & Schneider, R. Pliocene-Pleistocene variability of upwelling activity, productivity, and nutrient cycling in the Benguela region. *Geology* **37**, 871–874 (2009).
50. Kemp, A. E. S., Grigorov, I., Pearce, R. B. & Garabato, A. C. N. Migration of the Antarctic Polar front through the mid-Pleistocene transition: evidence and climatic implications. *Quat. Sci. Rev.* **29**, 1993–2009 (2010).
51. Cartagena-Sierra, A. et al. Latitudinal migrations of the subtropical front at the Agulhas Plateau through the Mid-Pleistocene Transition. *Paleoceanogr. Paleoclimatol.* **36**, <https://doi.org/10.1029/2020PA004084> (2021).
52. Nuber, S. et al. Indian Ocean salinity build-up primes deglacial ocean circulation recovery. *Nature* **617**, 306–311 (2023).
53. Staten, P. W., Lu, J., Grise, K. M., Davis, S. M. & Birner, T. Re-examining tropical expansion. *Nat. Clim. Change* **8**, 768–775 (2018).
54. Hu, Y., Huang, H. & Zhou, C. Widening and weakening of the Hadley circulation under global warming. *Sci. Bull.* **63**, 640–644 (2018).
55. Kushner, P. J., Held, I. M. & Delworth, T. L. Southern Hemisphere atmospheric circulation response to global warming. *J. Clim.* **14**, 2238–2249 (2001).
56. Kang, S. M. & Polvani, L. M. The interannual relationship between the latitude of the eddy-driven jet and the edge of the Hadley cell. *J. Clim.* **24**, 563–568 (2011).
57. Burls, N. J. et al. The Cape Town "Day Zero" drought and Hadley cell expansion. *npj Clim. Atmos. Sci.* **2**, 1–8 (2019).
58. Abell, J. T., Winckler, G., Anderson, R. F. & Herbert, T. D. Poleward and weakened westerlies during Pliocene warmth. *Nature* **589**, 70–75 (2021).
59. Mart'inez-Garcia, A. et al. Links between iron supply, marine productivity, sea surface temperature, and CO₂ over the last 1.1 Ma. *Paleoceanography* **24**, <https://doi.org/10.1029/2008PA001657> (2009).
60. Marlow, J. R., Lange, C. B., Wefer, G., Rosell-Mel' e, A. Upwelling intensification as part of the pliocene-pleistocene climate transition. *Technical Rep.* 10.1126/science.290.5500.2288. <http://science.sciencemag.org/> (2000).
61. Rosell-Mel' e, A., Mart'inez-Garcia, A. & McClymont, E. L. Persistent warmth across the Benguela upwelling system during the Pliocene epoch. *Earth Planet. Sci. Lett.* **386**, 10–20 (2014).
62. Rubbelke, C. B. et al. Plio-Pleistocene Southwest African Hydroclimate Modulated by Benguela and Indian Ocean Temperatures. *Geophys. Res. Lett.* **50**, 2023–103003 (2023).
63. Matmon, A. et al. New chronology for the south-ern Kalahari Group sediments with implications for sediment-cycle dynamics and early hominin occupation. *Quat. Res.* **84**, 118–132 (2015).
64. Blackwell, B. et al. Ages for the Early Stone Age deposits and an early Lechwe (Kobus leche) find at Groot Kloof (Northern Cape Province, South Africa). *Palaeoanthropol. Soc. Meeting Abstracts*, Memphis, 17–18 (2012).
65. Schefuß, E., Schouten, S., Jansen, J. H. F. & Sinninghe Damaste, J. S. African vegetation controlled by tropical sea surface temperatures in the mid-Pleistocene period. *Nature* **422**, 415–421 (2003).
66. Maslin, M. A. et al. East African climate pulses and early human evolution. Elsevier Ltd <https://doi.org/10.1016/j.quascirev.2014.06.012> (2014).

67. Lüdeck, T. et al. Persistent C3 vegetation accompanied Pliocene hominin evolution in the Malawi Rift (Chiwondo Beds, Malawi). *J. Hum. Evol.* **90**, 163–175 (2016).
68. Quinn, R. L. & Lepre, C. J. Contracting eastern African C4 grasslands during the extinction of *Paranthropus boisei*. *Sci. Rep.* **11** <https://doi.org/10.1038/s41598-021-86642-z> (2021).
69. Chazan, M. & Horwitz, L. K. in *Wonderwerk Cave and the Kathu Complex, South Africa*, (Beyin, A., Wright, D. K., Wilkins, J., Olszewski, D. I. eds.) 1749–1765. Springer, Cham <https://doi.org/10.1007/978-3-031-20290-2116>. (2023).
70. City of Cape Town. Water and Sanitation Department. Retrieved from http://resource.capetown.gov.za/documentcentre/Documents/Forms%2Cnotices%2Ctariffsandlists/Water_and_sanitation_restriction_Tariffs.pdf (2018).
71. City of Cape Town. Cape Town water strategy. Retrieved from <http://resource.capetown.gov.za/documentcentre/Documents/Citystrategies%2Cplansandframeworks/CapeTownDraftWaterStrategy2019PublicParticipation.pdf> (2019).
72. Rensburg, P. & Tortajada, C. An Assessment of the 2015–2017 Drought in Windhoek. *Front. Clim.* **3**, <https://doi.org/10.3389/fclim.2021.602962> (2021).
73. Otto, F. E. L. et al. Anthropogenic influence on the drivers of the Western Cape drought 2015–2017. *Environ. Res. Lett.* **13**, <https://doi.org/10.1088/1748-9326/aae9f9> (2018).
74. Sousa, P. M., Blamey, R. C., Reason, C. J. C., Ramos, A. M. & Trigo, R. M. The ‘Day Zero’ Cape Town drought and the poleward migration of moisture corridors. *Environ. Res. Lett.* **13**, <https://doi.org/10.1088/1748-9326/aaebc7> (2018).
75. Mahlalela, P. T., Blamey, R. C. & Reason, C. J. C. Mechanisms behind early winter rainfall variability in the southwestern Cape, South Africa. *Clim. Dyn.* **53**, 21–39 (2019).
76. Roffe, S. J., Steinkopf, J. & Fitchett, J. M. South African winter rainfall zone shifts: a comparison of seasonality metrics for Cape Town from 1841–1899 and 1933–2020. *Theor. Appl. Climatol.* **147**, 1229–1247 (2022).
77. Seager, R. et al. Climate variability and change of Mediterranean-type climates. *J. Clim.* **32**, 2887–2915 (2019).
78. Jeng, W. L. Higher plant n-alkane average chain length as an indicator of petrogenic hydrocarbon contamination in marine sediments. *Mar. Chem.* **102**, 242–251 (2006).
79. Sachse, D. et al. Molecular paleohydrology: interpreting the hydrogen-isotopic composition of lipid biomarkers from photosynthesizing organisms. *Annu. Rev. Earth Planet. Sci.* **40**, 221–249 (2012).
80. Inglis, G. N. et al. Biomarker approaches for reconstructing terrestrial environmental change. *Annu. Rev. Earth Planet. Sci.* **50**, 369–394 (2022).
81. Gao, L., Edwards, E. J., Zeng, Y. & Huang, Y. Major evolutionary trends in hydrogen isotope fractionation of vascular plant leaf waxes. *PLoS ONE* **9**, 112610 (2014).
82. Bhattacharya, T. et al. Expansion and Intensification of the North American Monsoon During the Pliocene. *AGU Adv.* **3** <https://doi.org/10.1029/2022AV000757> (2022).
83. Windler, G., Tierney, J. E., Zhu, J. & Poulsen, C. J. Unraveling glacial hydroclimate in the Indo-Pacific Warm Pool: Perspectives from water isotopes. *Paleoceanogr. Paleoclimatol.* **35**, 2020–003985 (2020).
84. Jolliffe, I. T. & Morgan, B. Principal component analysis and exploratory factor analysis. *Stat. methods Med. Res.* **1**, 69–95 (1992).
85. O’Rourke, N. & Hatcher, L. A. Step-by-step approach to using sas for factor analysis and structural equation modeling, 2nd edn. (SAS Institute Inc, USA). <https://doi.org/10.1002/9781119111931.ch159> (2013).
86. Pedregosa, F. et al. Scikit-learn: machine learning in Python. *J. Mach. Learn. Res.* **12**, 2825–2830 (2011).
87. Valdes, P. J. et al. The BRIDGE HadCM3 family of climate models: HadCM3@Bristol v1.0. *Geosci. Model Dev.* **10**, 3715–3743 (2017).
88. Cox, P. et al. The impact of new land surface physics on the GCM simulation of climate and climate sensitivity. *Clim. Dyn.* **15**, 183–203 (1999).
89. Hopcroft, P. O. & Valdes, P. J. Green Sahara tipping points in transient climate model simulations of the Holocene. *Environ. Res. Lett.* **17**, <https://doi.org/10.1088/1748-9326/ac7c2b> (2022).
90. Schneider, D. P., Deser, C., Fasullo, J. & Trenberth, K. E. Climate data guide spurs discovery and understanding. *Eos Trans. Am. Geophys. Union* **94**, 121–122 (2013).
91. Burls, N. J. & Reason, C. J. C. Sea surface temperature fronts in the midlatitude South Atlantic revealed by using microwave satellite data. *J. Geophys. Res. Oceans* **111**, <https://doi.org/10.1029/2005JC003133> (2006).
92. Durgadoo, J. V., Loveday, B. R., Reason, C. J. C., Penven, P. & Bias-toch, A. Agulhas leakage predominantly responds to the southern hemisphere westerlies. *J. Phys. Oceanogr.* **43**, 2113–2131 (2013).
93. Orsi, A. H., Whitworth, T. III. & Nowlin, W. D. Jr. On the meridional extent and fronts of the Antarctic Circumpolar Current. *Deep Sea Res. Part I Oceanogr. Res. Pap.* **42**, 641–673 (1995).
94. Belkin, I. M. & Gordon, A. L. Southern Ocean fronts from the Greenwich ian to Tasmania. *J. Geophys. Res. Oceans* **101**, 3675–3696 (1996).
95. Herries, A. I. R. Chronology of the Hominin Sites of Southern Africa. Oxford University Press, Oxford <https://doi.org/10.1093/acrefore/9780190854584.013.57> (2022).
96. Lehner, B. & Grill, G. Global river hydrography and network routing: baseline data and new approaches to study the world’s large river systems. *Hydrol. Process.* **27**, 2171–2186 (2013).

Acknowledgements

T.B. and C.R. acknowledge support from CAREER award OCE-2237502 and NSF P2C2 grant OCE-2103015. T.B. acknowledges support from Sloan Foundation Fellowship FG-2023-20259.

Author contributions

Conceptualization: C.R. and T.B. Data curation: C.R. Formal analysis: C.R. Funding acquisition: T.B. Investigation: C.R. Methodology: T.B., P.V., and A.F. Resources: T.B. Supervision: T.B. Visualization: C.R. Writing - original draft: C.R. Writing - Review and editing: C.R., T.B., E.M., H.F., and A.F.

Competing interests

The authors declare no competing interests.

Additional information

Supplementary information The online version contains supplementary material available at <https://doi.org/10.1038/s41467-025-58792-5>.

Correspondence and requests for materials should be addressed to Claire B. Rubbelke.

Peer review information *Nature Communications* thanks Catherine Beck, Enqing Huang and the other, anonymous, reviewer(s) for their contribution to the peer review of this work. A peer review file is available.

Reprints and permissions information is available at <http://www.nature.com/reprints>

Publisher’s note Springer Nature remains neutral with regard to jurisdictional claims in published maps and institutional affiliations.

Open Access This article is licensed under a Creative Commons Attribution-NonCommercial-NoDerivatives 4.0 International License, which permits any non-commercial use, sharing, distribution and reproduction in any medium or format, as long as you give appropriate credit to the original author(s) and the source, provide a link to the Creative Commons licence, and indicate if you modified the licensed material. You do not have permission under this licence to share adapted material derived from this article or parts of it. The images or other third party material in this article are included in the article's Creative Commons licence, unless indicated otherwise in a credit line to the material. If material is not included in the article's Creative Commons licence and your intended use is not permitted by statutory regulation or exceeds the permitted use, you will need to obtain permission directly from the copyright holder. To view a copy of this licence, visit <http://creativecommons.org/licenses/by-nc-nd/4.0/>.

© The Author(s) 2025